

Research Article

Characteristics of Pores under the Influence of Cyclic Cryogenic Liquid Carbon Dioxide Using Low-Field Nuclear Magnetic Resonance

Jizhao Xu,^{1,2,3} Cheng Zhai ,^{1,2,3} Lei Qin,^{1,2,3} Shangjian Wu,^{1,2,3} Yong Sun,^{1,2,3} and Ruowei Dong^{1,2,3}

¹State Key Laboratory of Coal Resources and Safe Mining, Xuzhou, Jiangsu 221116, China

²Key Laboratory of Coal Methane and Fire Control, Ministry of Education, China University of Mining and Technology, Xuzhou, Jiangsu 221116, China

³School of Safety Engineering, China University of Mining and Technology, Xuzhou 221116, China

Correspondence should be addressed to Cheng Zhai; greatzc@126.com

Received 25 October 2017; Revised 12 April 2018; Accepted 3 May 2018; Published 2 July 2018

Academic Editor: Fengshou Zhang

Copyright © 2018 Jizhao Xu et al. This is an open access article distributed under the Creative Commons Attribution License, which permits unrestricted use, distribution, and reproduction in any medium, provided the original work is properly cited.

The enhancement of coalbed methane extraction by repeatedly injecting CO₂ has been investigated for many decades, mostly focusing on the fracturing and flooding effect in numerous lab experiments, simulations, and field applications, whereas the effect of the accompanying heat transfer during cyclic liquid CO₂ (LCO₂) injection has rarely been studied. In this paper, the influence of the cyclic injection of cryogenic LCO₂ with different cycle numbers and time on the coal pore variation was explored using low-field nuclear magnetic resonance to extract the T_2 spectral information. The results have shown that as the cycle number increased, the adsorbed water (AW) decreased while the capillary water (CW) and bulk water (BW) values increased, and the pore volumes were magnified greatly based on the tendencies of fitted polynomial curves of I_{sa1} values and fitted exponential curve of I_{sa2} values. With increasing cycle time, the increase ratios of AW, CW, and BW were not independent but mutually influenced, and the I_{sa1} values approximately displayed a “rapid increase-slow increase” tendency, while I_{sa2} roughly showed fluctuating or “increase-decrease” tendencies. The changes in the IWS and FWS showed that the increased pore connectivity could allow more water to infiltrate into the pores at the saturation state and accelerate the removal of fluid water during the centrifugation state. The φ_e and φ_r variations indicated that longer cycle time coupled with a larger cycle number could cause damage generation and enhance the pore connectivity.

1. Introduction

Coalbed methane (CBM) is mainly formed during a long epoch of coalification stages and reserves in the coal seams under the effect of stratum sedimentation accompanied by high temperature and pressure [1–4]. The detectable CBM content in the reservoirs is abundant, and its recovery has attracted interests and concerns from many governments, researchers, and entrepreneurs, due to its higher calorific value, abundant content, and less environmentally damaging nature [5, 6]. However, the permeability of most Chinese coal seams is generally three orders of magnitude lower than that of the San Juan basin, which is unsatisfactory for effective gas

extraction merely based on its original conditions [7–9]. Therefore, it is necessary to explore possible ways to improve the permeability.

Enhanced CBM (ECBM) recovery by injecting CO₂ along with amounts of proppants into the reservoirs along the fracture wells has been proposed and developed in some countries such as the United States [10, 11], Canada [12, 13], China [14, 15], and Japan [16, 17]; the reported results have all suggested that CO₂-ECBM has a significant application feasibility and that this method could increase the extraction efficiency by enhancing the permeability of reservoirs. In particular, liquid CO₂ (LCO₂) has been widely applied in the field of ECBM recovery [18]. LCO₂ has a

large liquid gas expansion ratio of 1:557 at 273 K and 1 atm, which can be used to generate huge gas pressures in confined spaces [19]. Cao et al. [20] studied the application of CO₂ gas fracturing in low-permeability gassy coal seams using the CARDOX system, which could cause the LCO₂ to form a high-pressure gas, and the results indicated that the permeability and methane drainage effectiveness were significantly improved. The larger adsorption capacity could help CO₂ compete with CH₄ to adsorb on the coal matrix, which finally converts a huge volume of adsorbed CH₄ to the free state [21, 22]. The complete compatibility with the matrix could avoid some reservoir damages, and the formed acidic species with lower pH values might prevent iron hydroxides from forming, buffer against clay reactions, and reduce the flow resistance of gas [23, 24]. Meanwhile, the geological sequestration of CO₂ could be achieved to some extent [25, 26].

Generally, the latent heat of evaporation for LCO₂ is 347 kJ/kg; therefore, it can adsorb a considerable amount of heat from the surroundings. When sufficient amounts of LCO₂ are injected in the boreholes, the heat transfer will occur at the contact surface between the LCO₂ and the coal matrix. A previous study has shown that the temperature of coals decreased obviously and even to less than -18°C when the core was contacted with LCO₂ media, causing the matrix to shrink [19]. A temperature gradient would be formed due to the high inherent temperature of the surrounding coal matrix, and a temperature stress was generated, accompanying one cycle of the “freeze-thaw” (“F-T”) process, which might induce some damage to occur in the coals [27]. The strengths of six sandstones under the effect of a cyclic F-T process deteriorated significantly [28]. Zhai et al. [29] studied consecutive F-T cycles on coal pore structure deterioration by using a compressor and a condenser, and the results from low-field nuclear magnetic resonance (LF-NMR) and scanning electron microscopy showed that the coal samples were significantly destroyed by F-T cycles, with numerous cracks generated on the coal surfaces. The F-T cycle number decreased the mechanical properties of rocks or cement materials, including shear strength [30], uniaxial compressive strength [31, 32], elastic modulus [33, 34], and P-wave velocity [35–37], and the integrity loss of the rocks was verified by a decay function [38]. Xu et al. proved the feasibility of cryogenic effects from cyclic LCO₂ fracturing [19] and investigated the influence of F-T effect on the pore variations of coal with different ranks [27], and the results all showed that the cyclic F-T process with LCO₂ had significant effects on the pore enhancement.

The mentioned publications mostly focused on the deterioration of the F-T effect with different cycle numbers, and rarely considering other cyclic parameters. In this paper, the influence of LCO₂ with different cycle numbers and time on the pore variation was studied, where the experimental subjects were six cores drilled from the same coal block. The methodology of pore measurement is introduced in Section 2, and some of the materials and equipment are described in Section 3. Finally, the experimental results are analyzed in Section 4.

2. Methodology

In general, the porous coal is composed of two subsystems, the coal matrix system and the fracture system, in which there are several states for CBM occurrence: trapped gas within the matrix pores, adsorption gas within micropores (<2 nm), and dissociative gas and dissolved gas in water within the fractures [39–41]. The diffusion phase in the matrix is determined by the concentration gradient, while the seepage phase in the cleats or fractures influences the gas extraction efficiency considerably [42, 43]. Porosity and permeability are two important evaluation indices to measure the volume of reserve gas and the seepage features of coals, respectively [44, 45]. Porosity is usually considered as the void spaces within the coal matrix and represents the capacity of coals to retain fluids, such as liquid or gas, which then indicates that a highly porous reservoir has a great potential to reserve abundant gas [46, 47]. The property determining the fluid flow ability through the coals via the interconnection of the pore spaces is known as permeability, which greatly influences the transport characteristics of CBM, such as migration within the matrix and flow from the matrix to the cleats or fractures [48].

Currently, the measurement methods for the petrophysical properties of coal, such as scanning electron microscopy (SEM) [49], optical microscopy, or transmission electron microscopy [50], usually display the surface morphology and pore size distribution qualitatively. The quantitative measurements, including gas adsorption [51], mercury intrusion porosimetry (MIP) [52], micro-X-ray tomography [53], and small-angle X-ray scattering or neutron scattering (SAXS/SANS) methods [54], could show the detailed information of the pores from a numerical aspect. However, these methods always have limited measurement ranges for the pore size as well as low efficiency and they cause damage to the pore structures [55]. Due to its properties of being nondestructive and highly efficient and having large test ranges, low-field nuclear magnetic resonance (LF-NMR) has been provided as an alternative measurement technique to obtain internal pore information for coal.

Water is generally the medium used to characterize the internal void spaces of porous media; the net magnetization of a hydrogen atom or proton ¹H from water-saturated coal placed in the sample chamber refers to an attenuation curve between signal amplitude and relaxation time using the Carr-Purcell-Meiboom-Gill (CPMG) spin-echo pulse sequence, which will be recorded by LF-NMR under the magnetic phenomenon [27, 52, 55] (shown in Figure 1). The signal amplitude is positively correlated to the proton ¹H number, which indirectly corresponds to the internal water content and therefore the pore spaces, that is, the porosity. Compared to the water kinetics from the T₂ spectra at the saturation condition, the kinetics from the T₂ spectra under the centrifugation condition are always different, and the longer T₂ values represent the mobile water molecules while the shorter values represent the irreducible water; thus, the entire T₂ spectrum could characterize the pore distribution. The amplitude values are proportional to

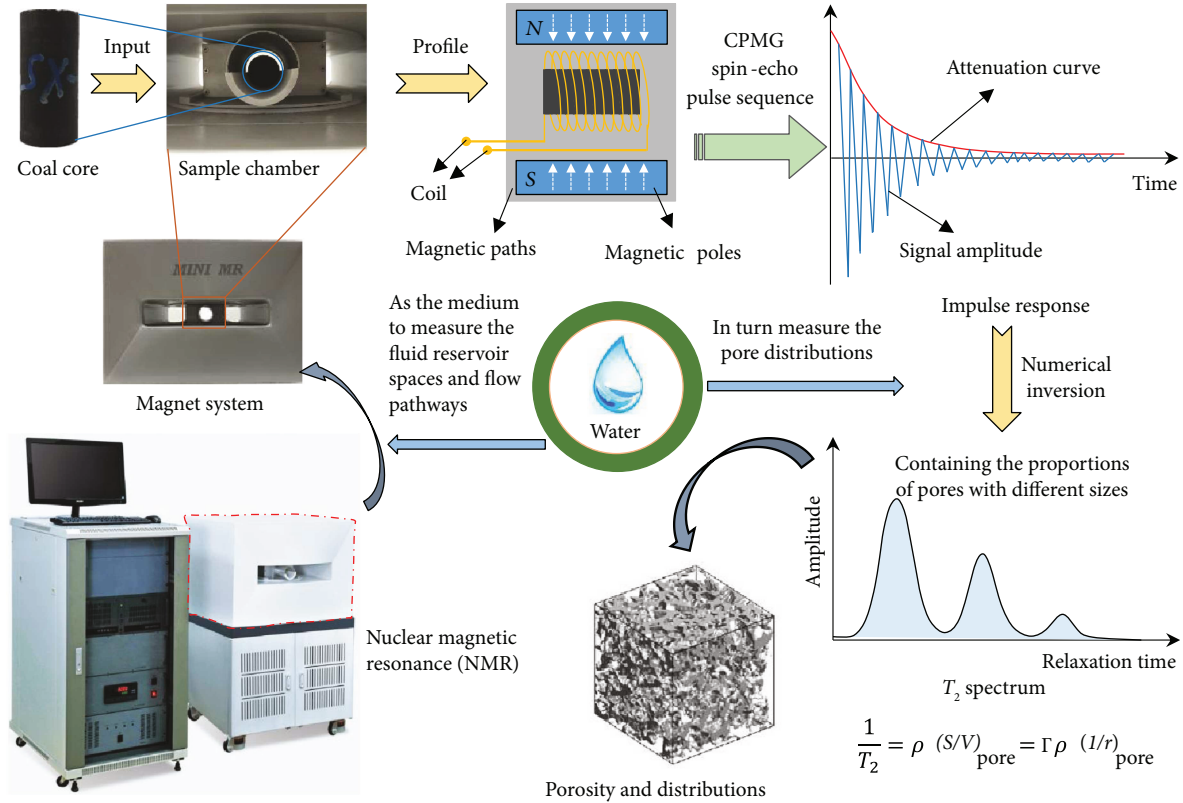


FIGURE 1: The measurement principle and process of LF-NMR.

the ratio of the pore surface to the pore volume according to Kleinberg et al. [56]:

$$\frac{1}{T_2} = \rho \left(\frac{S}{V} \right)_{\text{pore}} = \Gamma \rho \left(\frac{1}{r} \right)_{\text{pore}}, \quad (1)$$

where ρ is the surface relaxivity occurring at the mineral surface in $\mu\text{m/s}$; $(S/V)_{\text{pore}}$ is the surface to volume of the pore in μm^{-1} ; r is the pore radius in μm ; and Γ is a pore geometry constant.

3. Materials and Equipment

3.1. Coal Core Preparation. All six cores were drilled from the same coal block that came from Datong Coal Mine, Shanxi province, China, and their shapes are cylinders with an approximate diameter of 25 mm and an approximate length of 50 mm, as shown in Figure 2. These cores were labeled $sx-i$ ($i=1, 2, \dots, 6$). The proximate analysis results showed that cores $sx-i$ had a moisture value of 4.83%, ash yield value of 7.3%, volatile matter dry ash-free basis value of 29.64%, and fixed carbon content value of 58.23%. The $R_{o,\text{max}}$ value is 0.43, with values of 75.3% for vitrinite, 18.6% for inertinite, 2.7% for exinite, and 5.3% for minerals [57].

3.2. Experimental System and Procedures. According to previous studies [19, 27], an innovative experimental system (shown in Figure 3) comprised three components: a

cryogenic system, an LCO_2 injection system, and a data monitoring system. The first subsystem provides the cryogenic environment during the LCO_2 injection process, and the thermal insulation material around the chamber is used to maintain the internal low-temperature condition. The pressure relief valve is used to relieve the excess gas pressure for safety. The second subsystem could constantly inject LCO_2 into the chamber by using a pump. The function of the third subsystem mainly records the corresponding data during the experimental process with a pressure sensor and thermocouple to express the gas pressure and temperature, respectively.

During the pretest and posttest processing, the pore size and distributions of cores were tested by an LF-NMR (mini MR60) manufactured from Niumag Analytical Instrument Corporation, Suzhou, China, which has a magnetic field of 0.51 T, maximum sampling frequency of 333 kHz, and maximum echo number of 20000. Next, its auxiliary equipment, such as a vacuum drying oven (DHG-9023A), vacuum water saturation device (NEL-VJH), and rock centrifuge (TG16-WS), is also used to cause the cores to undergo the “drying-saturation-centrifugation” process for the purpose of obtaining the related T_2 spectra under the saturation and centrifugation conditions.

LF-NMR has a strict working temperature of 305 K for the purpose of accurate T_2 spectral measurement, and its sample scanning times were set at 64. The ambient (room) temperature and relative humidity were 298 K and 40%, respectively, and the drying temperature was set at 313 K.

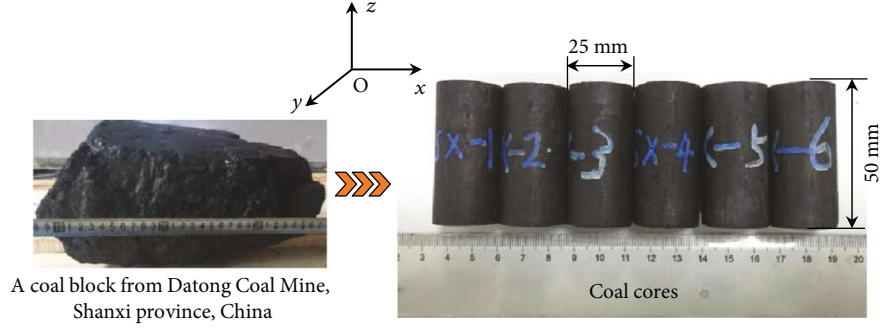


FIGURE 2: Images of coal block and drilled cores.

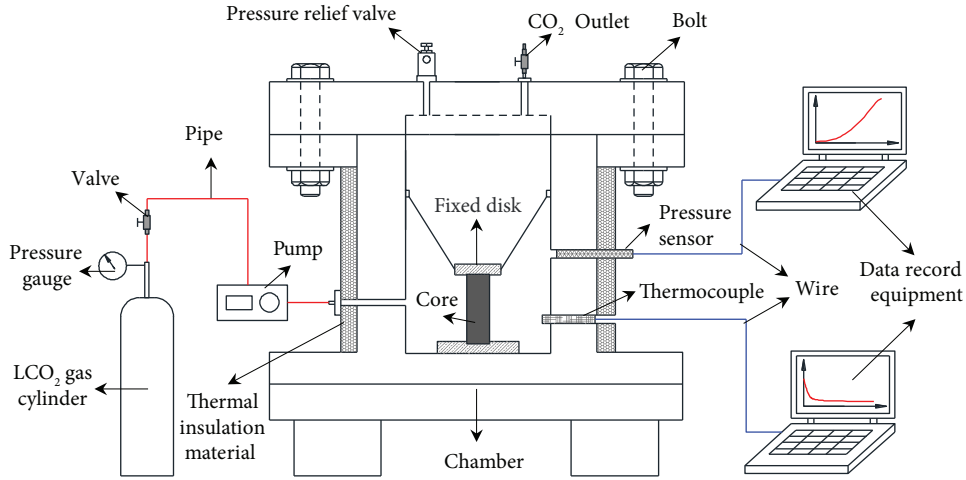


FIGURE 3: Sketch image of the experimental system.

TABLE 1: Experimental design of six cores.

Core number	Cycle number	LCO ₂ injection (min)	Normal temperature (min)	Total cycle time (min)
sx-1		5	5	10
sx-2		10	10	20
sx-3	5, 10, 15, 20,	15	15	30
sx-4	25	20	20	40
sx-5		25	25	50
sx-6		30	30	60

The experimental design is listed in Table 1, in which the cores were alternately placed in the cryogenic and the normal temperature environment to simulate the cyclic thermal interaction process. Initially, the weights of dried cores were tested by a balance, and then, they were immersed into distilled water for 24 hr to reach their saturation state. The saturated cores were measured by LF-NMR and a balance to obtain their original T_2 spectra and weights, respectively, for the saturation condition; next, the cores were centrifuged via rock centrifuge for 1.5 hr to remove the movable water and generate the centrifuged core state, and the original T_2 spectra and weights for the centrifugation condition

were measured by LF-NMR and a balance, respectively. Next, these cores were immersed into distilled water to ensure their saturation; then, they were packaged with a thin film and placed in a precooled chamber; LCO₂ was injected from the cylinder into the chamber; the cryogenic cores were then placed in a normal-temperature environment; and the durations for these steps are all listed in Table 1. Considering the water runoff, the cores affected by one cycle were then processed according to the flow path of “saturation-measurement-centrifugation-measurement.” Finally, the entire experiment was completed on the basis of the above testing process.

4. Results and Analysis

4.1. T_2 Spectral Analysis. Some T_2 spectra under the saturation and centrifugation conditions were obtained after different cycles of the LCO₂ injection process. Due to the similarity of the curves, core sx-1 was selected for the study of T_2 spectral changes along the relaxation time, and the distributions of the T_2 spectra at the initial state, after 15 cycles and after 25 cycles under two conditions, are shown in Figure 4. As seen in Figure 4(a), the amplitude peak values increased after different numbers of cycles of LCO₂ injection compared to those values at the initial state and

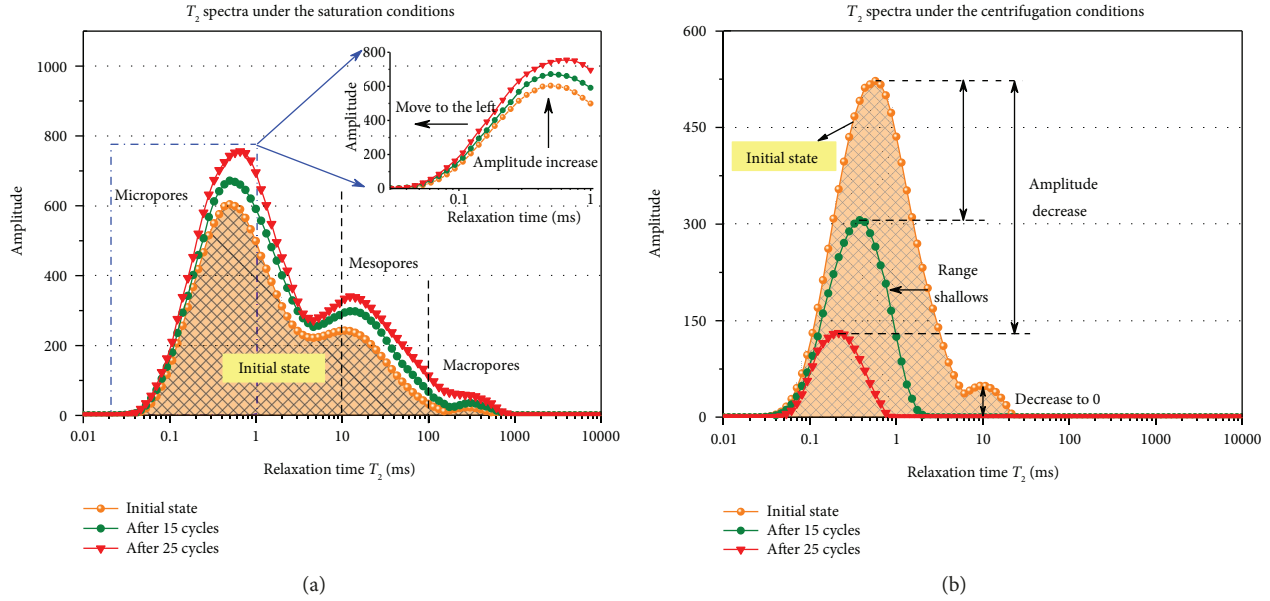


FIGURE 4: T_2 spectral curves of core sx-1 under the saturation and centrifugation conditions.

the amplitude increase was positively correlated to the cycle number; the amplitude values decreased with an increasing number of cycles of LCO₂ injection, and the decrement was negatively correlated to the cycle numbers. The T_2 spectra of the water-saturated cores expressed three distinct peaks, and from left to right, the corresponding pore sizes were micropores, mesopores, and macropores [19, 27, 55, 58], which indicated that the distilled water occupied approximately all the open or semiopen pores; the increased amplitude values and widened T_2 ranges all showed that the pore size and distributions varied greatly after different numbers of cycles of LCO₂ injection. The greater the amplitude increase and the larger the T_2 coverage, the greater the water volume and pore spaces. Meanwhile, the T_2 curves of the centrifuged cores showed two peaks or one peak, which indicated that the water in the larger pore sizes was removed and that the decreased amplitude value and the narrowing T_2 coverage all meant that the pore connectivity increased after different numbers of cycles of LCO₂ injection.

4.2. Variations of Three Types of Water in Cores. According to Dillinger and Esteban and Olatinsu et al. [59, 60], the T_2 curves of saturated cores usually contain some information about the relationship between water types and pores with different sizes; in general, the relaxation time less than 10 ms, dependent on the surface relaxation from the micropore walls, represents the adsorbed water (AW); the relaxation time from 10 ms to 100 ms, attributed to the surface relaxation in the mesopores, denotes the capillary water (CW); and the relaxation time larger than 100 ms (up to 10,000 ms), corresponding to the macropores, signifies the bulk water (BW). Figure 5(a) shows the variations of AW, CW, and BW for cores sx-1 and sx-4 with increasing cycle numbers. The three types of water proportions varied differently; for example, the proportions of BW all increased,

the CW proportion increased, and the AW proportion decreased for core sx-4, while the maximum CW proportion and the minimum AW proportion of core sx-1 were present after 20 cycles. Figures 5(b)–5(d) show the variations of AW, CW, and BW, respectively. As the cycle number increased, the AW of six cores all expressed decreasing trends of different amplitudes, and the cores' CW and BW increased in the opposite direction. The values of AW, CW, and BW were within the range of [0.812, 0.84], [0.143, 0.173], and [0.007, 0.017], respectively, at the initial state; then, the values correspondingly changed to the ranges of [0.759, 0.802], [0.172, 0.193], and [0.02, 0.05] after 15 cycles of LCO₂ injection and of [0.731, 0.791], [0.176, 0.202], and [0.033, 0.067] after 25 cycles of LCO₂ injection. The changes indicated that the water proportion variations were comprehensively impacted by the changes of pore sizes; additionally, the AW decrease did not mean that the micropore numbers decreased but rather that those pores transformed into mesopores under a cyclic “shrink-swell” effect, causing unallowable deformation generation and internal damage within the coal matrix. In the meantime, the partial CW freezing could enlarge the size of the mesopores to form macropores due to the ice-wedge effect. The longer LCO₂ injection time might cause the CW and BW to freeze completely, providing more opportunities for the macropore number to increase.

Figure 5 shows the distributions of the three types of water values; however, due to the different initial values, the subsequent values changed greatly on the basis of the larger values; thus, it is necessary to estimate the increase ratios of AW, CW, and BW compared to the initial values under different cycle numbers and cycle time, and their variations are each shown in Figure 6. On the one hand, the increase ratios of AW displayed “decrease-increase-decrease” trends, while those of CW showed an “increase-decrease-increase” tendency after 5 cycles and 10 cycles; on the other hand,

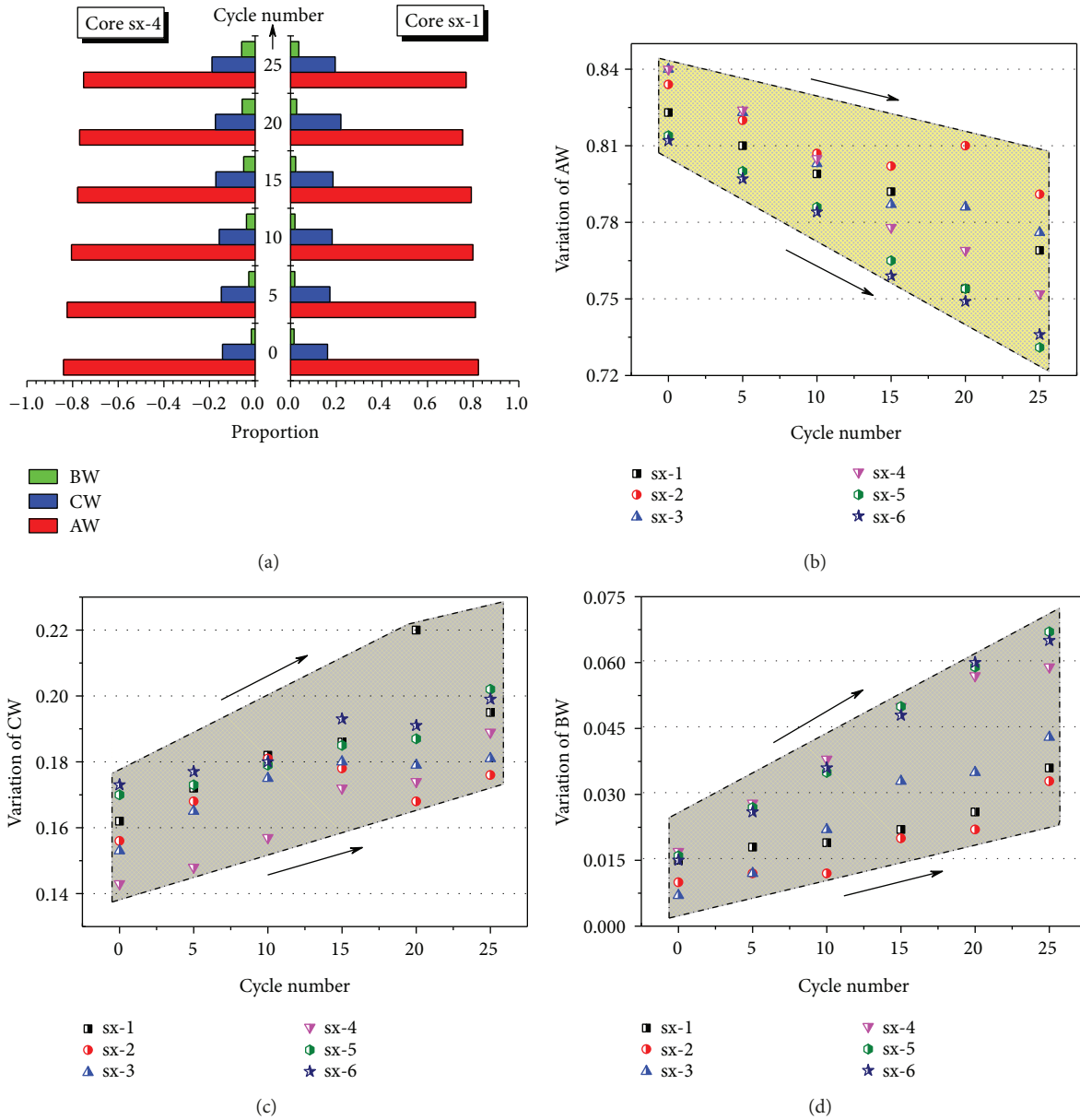


FIGURE 5: Changes of AW, CW, and BW for different cores: (a) proportion of AW, CW, and BW for cores sx-1 and sx-4; (b), (c), and (d) mean the variations of AW, CW, and BW, respectively, with increasing cycle number.

the increase ratios of AW and CW all changed adversely with higher cycle numbers; however, the increase ratios of BW approximately showed similar “increase-decrease-increase” changes as the cycle time increased.

As seen in Figures 6(a)–6(c), the largest increase ratios of AW (negative values) and the smallest increase ratios of CW and BW after 5 cycles all indicated that the lower cycle numbers could partly cause the internal pores with different sizes to change with small amplitude and that the increase ratios of three types of water varied greatly with large amplitudes after the longer cycle time. The increase ratios of water after 20 cycles and 25 cycles had the largest changes that accompanied the sharp increase or decrease. These variations and differences all indicated that the water increase ratios were positively correlated to the cycle number and that the larger

cycle numbers could freeze the saturated water and shrink the coal matrix for larger times, inducing more “unallowed damages or deformations” to form and accumulate with circulation, which would cause many transformations among pores with different sizes; thus, LCO₂ injection with more cycles had greater superiority to enhance the fracture results by producing many macropores to provide free pathways for fluids. Moreover, the three water increase ratio variations were not independent but were affected mutually, as shown in Figure 6(d). The greater BW increase ratios, representing the larger BW proportion, signified a larger transformation of mesopores due to the ice-wedge effect; meanwhile, the cyclic F-T process also facilitated the growing amount of mesopores and the corresponding CW proportions and increase ratios also increased. After the larger cycle numbers,

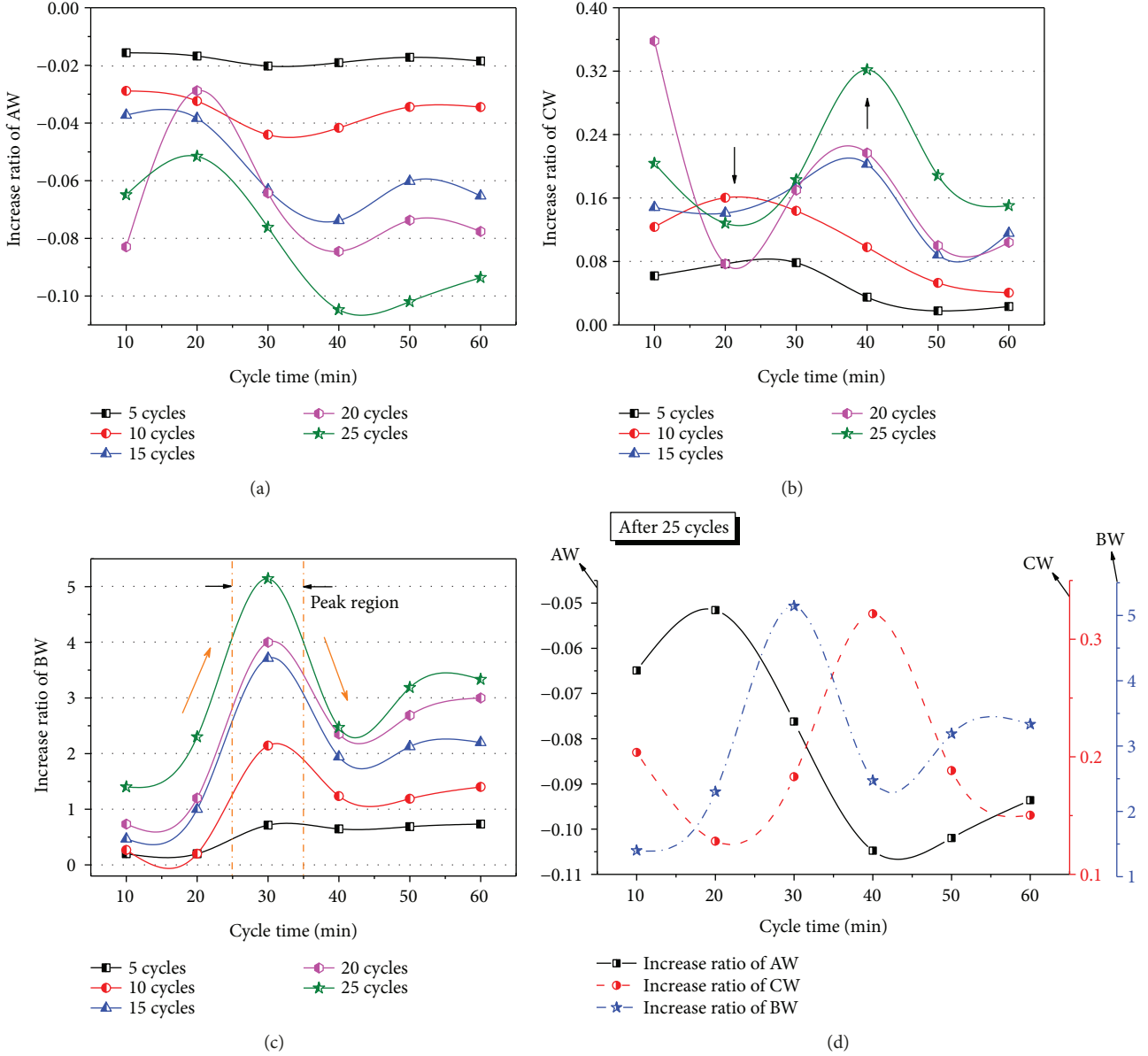


FIGURE 6: Increase ratio of AW, CW, and BW for six cores after different cycle time and cycle numbers.

the AW increase ratios (negative values) were minimized under the cycle time of 40 min, which was true for the maximum CW increase ratios as well, while the maximum increase ratios of BW were at the cycle time of 30 min. This enhancement analysis could provide some information to improve the LCO₂ cyclic injection process.

4.3. Analysis of Spectral Areas. The coverage under a T_2 spectrum commonly indicates the pore volumes including the pores with different sizes where water could infiltrate. The spectral area is calculated by an integration of the amplitude along the relaxation time, and a greater amplitude with wider range indicates a larger internal pore volume at a certain time duration. To obtain the information of pore volume changes from the T_2 spectra, an increase ratio of spectral area I_{saij} was adopted to characterize the area enhancement due to the

various initial values of the different cores. The function of I_{saij} was deduced as follows:

$$I_{saij} = \frac{\Delta S_{ij}}{S_{inj}} = \frac{S_{poij} - S_{inj}}{S_{inj}}, \quad i = 5, 10, \dots, 25, j = 1, 2, \quad (2)$$

where I_{saij} means the increase ratio of the spectral area under saturation and centrifugation states after the i th cycle injection; S_{poij} and S_{inj} represent the spectral areas after the i th cycle of LCO₂ injection and the initial areas, respectively; ΔS_{ij} is the difference between S_{poij} and S_{inj} ; and $j = 1, 2$ means the two states of saturation and centrifugation.

As seen in Figures 7(a) and 7(b), the I_{sa1} of six cores increased with different amplitudes with the increasing cycle number, which indicated that the internal pore volumes all

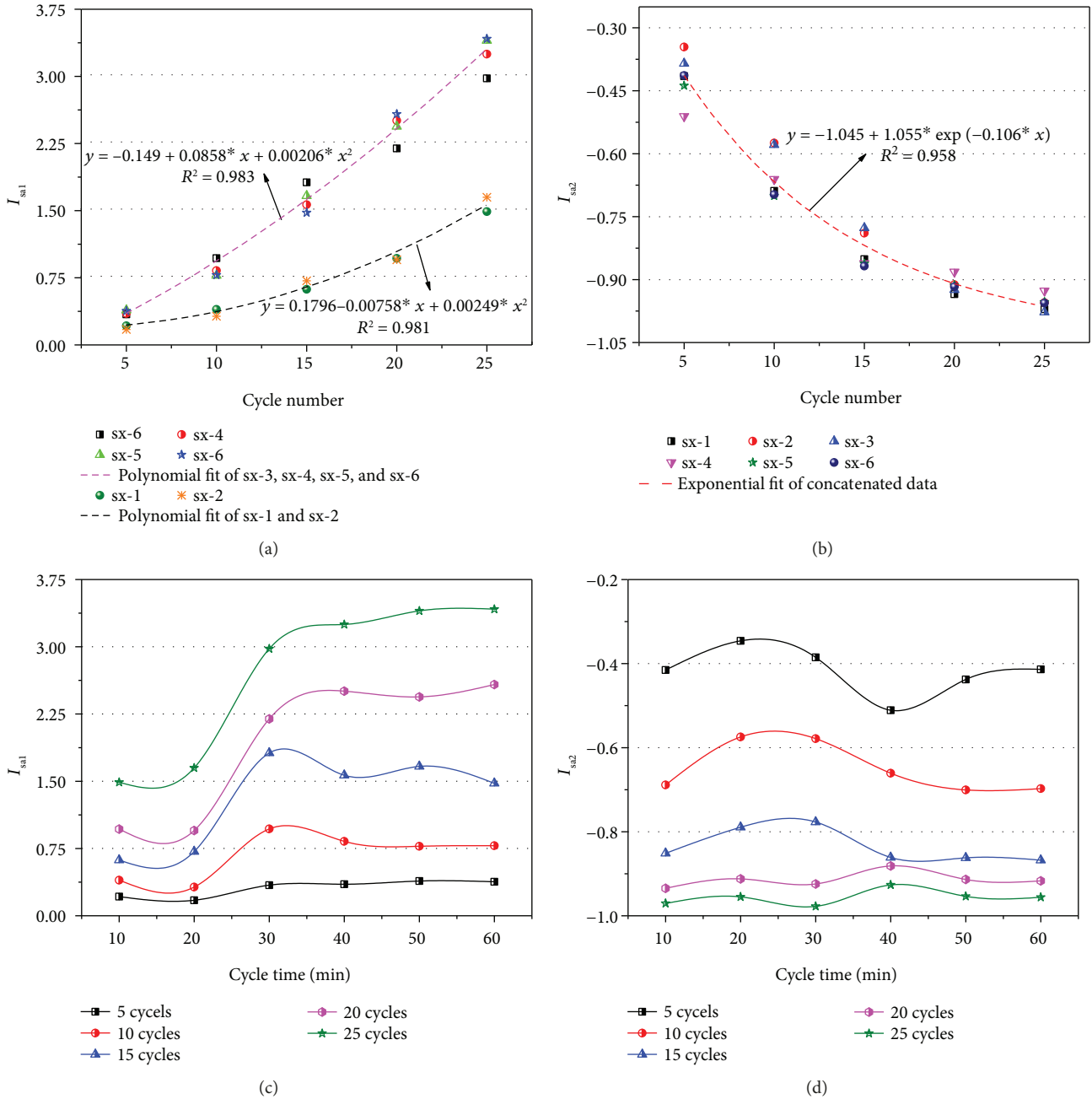


FIGURE 7: Variations of I_{sa1} and I_{sa2} with increasing cycle number and cycle time.

enlarged after the cyclic F-T effect from LCO₂ injection with different cycles. The connectivity among pores was enhanced in the form of uplifting amplitude peaks and widening curve coverage, enabling the water to immerse in the pore spaces, and the greater I_{sa1} meant the greater enhancement of pore volume and connectivity. Moreover, the I_{sa1} scatters were distributed with two different regions at the dividing cycle time of 20 min: the I_{sa1} scatters of cores affected for less than 20 min cycle time increased slowly, whereas those effected for more than 20 min cycle time increased greatly. Due to the fewer differences among their values at a certain cycle number within each region, the method of concatenated fit was

used to approximate the variation tendency. The data in the two regions were all fitted by polynomial curves with good fit coefficients larger than 0.98:

$$\begin{aligned} \text{Small } I_{sa1} \text{ region : } y &= -0.149 + 0.0858x \\ &+ 0.00206x^2 \quad (R^2 = 0.983), \\ \text{Large } I_{sa1} \text{ region : } y &= 0.1796 - 0.00758x \\ &+ 0.00249x^2 \quad (R^2 = 0.981). \end{aligned} \quad (3)$$

In contrast, the I_{sa2} values of the six cores in Figure 7(b) all decreased as the cycle number increased, and these

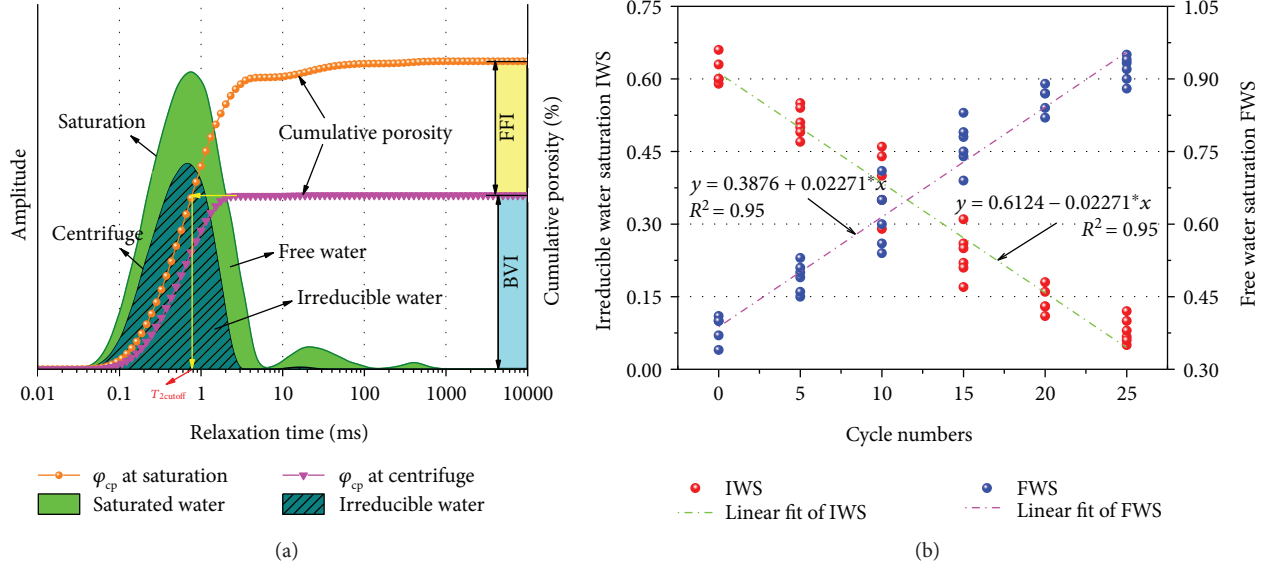


FIGURE 8: Diagram of the porosity division dependent on the T_2 spectra (a) and scatters and the fitting lines of IWS and FWS (b).

scatters were all fitted as exponential curves, with their concatenated data fit curve shown as follows:

$$y = -1.045 + 1.055 \cdot \exp(-0.1026 \cdot x) \quad (R^2 = 0.958). \quad (4)$$

The fit curves of the I_{sa1} and I_{sa2} values all indicated that the pore volumes magnified more greatly as the cycle number increased. The cyclic effect of the F-T process would cause many deformations or damage to be generated around the pore walls or tips, and the physical parameters of whole cores decreased; thus, the pore spaces will easily be enlarged under the coupled effect of temperature stress and ice extrusion, which would cause more water to occupy the pores under the saturation state and to be removed from the free spaces under the centrifugation condition.

Figures 7(c) and 7(d) both show the variations of I_{sa1} and I_{sa2} with increasing cycle time. On the whole, the I_{sa1} increments and I_{sa2} decrements after larger cycles of LCO₂ injection were all greater than those after LCO₂ injection with smaller cycles, which was well consistent with (3) and (4). Moreover, as the cycle time increased, the I_{sa1} values approximately displayed a “rapid increase-slow increase” tendency, while I_{sa2} roughly showed an “increase-decrease” tendency for short cycles and double “increase-decrease” trends for long cycles. In addition, the I_{sa1} values with longer cycle time increased much more than those with a shorter cycle time; both I_{sa2} variations indicated that the number of open or semiopen pores increased, causing more free water to be removed during the centrifugation process. The potentials indicated that the longer freezing time might cause the matrix to conduct the heat and cause the saturated water occupying the pores with different sizes to freeze into ice completely, after which the pore volumes would be magnified much more due to the ice-extrusion and ice-wedge effects.

4.4. Porosity Analysis. The weight method was used to calculate the porosity under the water saturation and centrifugation conditions. The original weight of the completely dried core was regarded as M_{dry} , and the water-saturated cores and centrifuged cores after LCO₂ treatment with different cycle parameters were regarded as M_{sat} and M_{cen} , respectively. Thus, the corresponding porosity ϕ could be calculated as follows [19, 27]:

$$\phi = \frac{V_{water}}{V_{core}} = \begin{cases} \frac{(M_{sat} - M_{dry})}{V_{core}} & (\text{saturation}), \\ \frac{(M_{cen} - M_{dry})}{V_{core}} & (\text{centrifuge}), \end{cases} \quad (5)$$

where V_{water} and V_{core} represent the water volume in pores and the core volume (cm^3), respectively, $(M_{sat} - M_{dry})/V_{core}$ is for saturation, $(M_{cen} - M_{dry})/V_{core}$ is for centrifugation, and the water density is 1 g/cm^3 .

According to [27, 57, 61, 62], the T_2 spectra under the saturation and centrifugation conditions also characterize the variation of three kinds of porosity, such as total porosity (ϕ_t), effective porosity (ϕ_e), and residual porosity (ϕ_r). Figure 8(a) shows the diagram of porosity division dependent on the T_2 spectra. All the amplitude values were processed using normalization calculation, and the cumulative porosity under saturation was deemed to be ϕ_t while the cumulative porosity under centrifugation was considered to be ϕ_r ; thus, the difference of ϕ_r from ϕ_t was ϕ_e . Moreover, the spectral area of the centrifuged core always represents the remaining water volume in the pores, namely, the bound pore volume; thus, the ratio of the spectral area at centrifugation to that at saturation, referred to as the irreducible water saturation (IWS), might be adopted to characterize the proportion variation of bound pore volume under the effect of the LCO₂ injection, which also expresses the volume changes of the

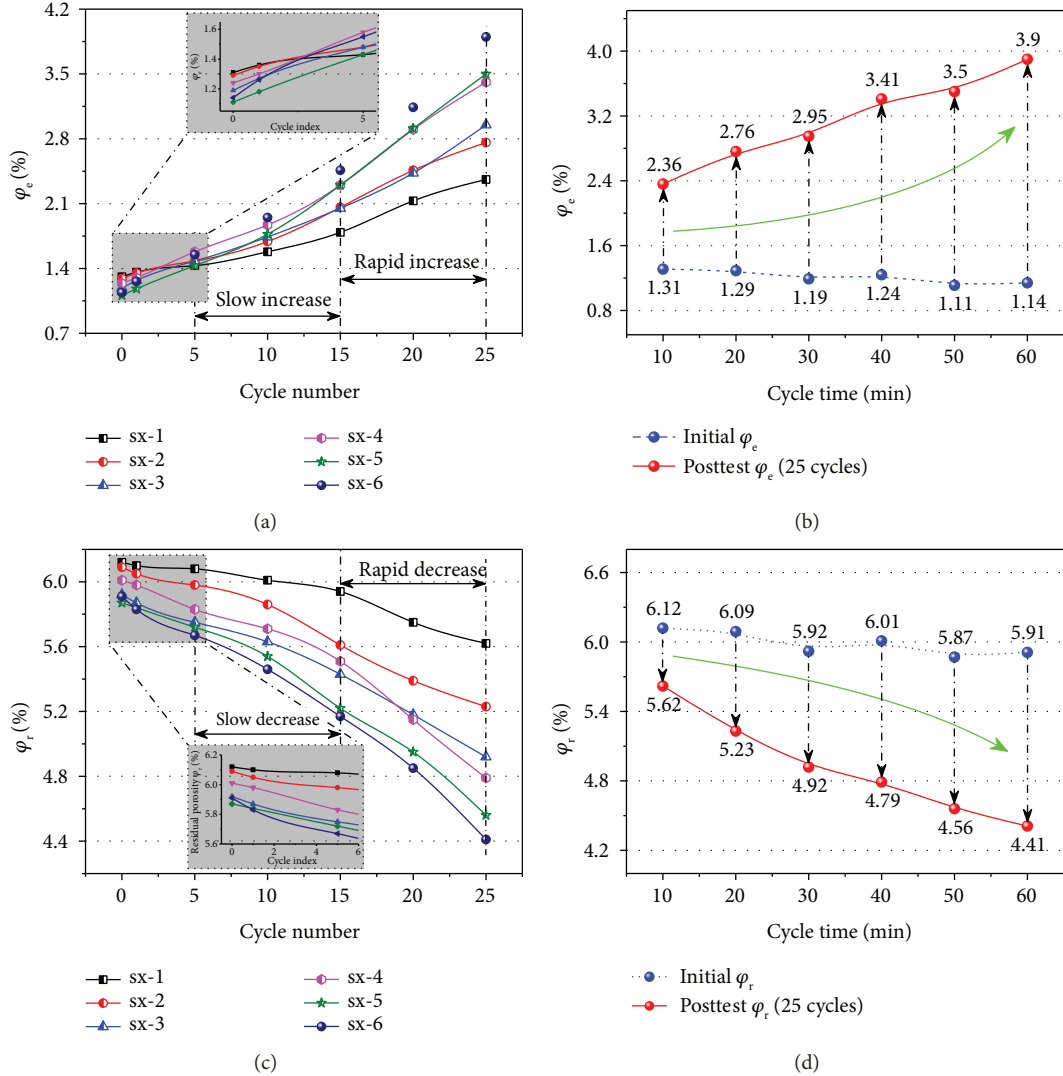


FIGURE 9: Variations in the φ_e and φ_r values of the six cores after different cycle time and cycle numbers.

connected pore. Thus, the equations of IWS and free water saturation (FWS) were deduced as follows:

$$\begin{aligned} \text{IWS} &= \frac{S_{\text{cen}}}{S_{\text{sat}}}, \\ \text{FWS} &= \frac{S_{\text{sat}} - S_{\text{cen}}}{S_{\text{sat}}} = 1 - \frac{S_{\text{cen}}}{S_{\text{sat}}}. \end{aligned} \quad (6)$$

As seen in Figure 8(b), all the IWS and FWS values of the six cores show similar changes with increasing cycle number. The IWS values decreased as the cycle number increased, which was consistent with the tendency of increased amplitude and widened T_2 spectral coverage under the saturation condition. Meanwhile, the FWS values were negatively correlated to the cycle number, which indicated that more fluid water was removed from the saturated cores, which in turn indicated that the free pore volume and space increased after the cyclic LCO₂ application. Moreover, there were linear

relationships between the two kinds of corresponding concatenated values and cycle number:

$$\begin{aligned} \text{IWS} : y &= 0.3876 + 0.02271 * x (R^2 = 0.95), \\ \text{FWS} : y &= 0.6124 - 0.02271 * x (R^2 = 0.95). \end{aligned} \quad (7)$$

These two linear fit curves all have great fit coefficients of 0.95, and the potentials of IWS and FWS indicated that the increments and decrements were relatively variable; as the total pore volume increased, the amounts of immersed water or removed water were also influenced by several factors, such as the chemical and physical properties of pore walls, the clay content, and the mineral distributions.

Dependent on (5) and Figure 8(a), the variations in φ_e and φ_r after LCO₂ treatment with different cycle parameters are shown in Figure 9. Figures 9(a) and 9(b) show that the φ_e values change with the increasing cycle parameters, and Figures 9(c) and 9(d) display the variations in the φ_r values as the cycle parameters increase. All the φ_e values positively

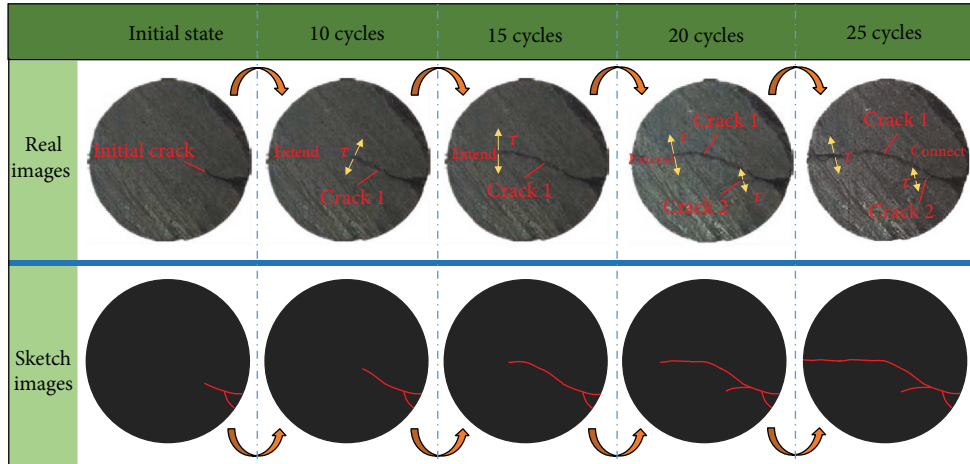


FIGURE 10: Propagation of a surface crack of sx-1 in forms of real images and sketch images.

correlated to the cycle parameters and had a “slow increase-rapid increase” tendency, whereas the φ_r values were negatively related to the cycle parameters and showed a “slow decrease-rapid decrease” trend. With a case study of core sx-3, the φ_e increment was 0.26% with an increase ratio of 46.2% after 10 cycle numbers, while it was 1.76% with an increase ratio of 176% after 25 cycle numbers. However, the φ_r decrement was 0.29% (decrease ratio of 4.9%) after 10 cycle numbers and 1% (decrease ratio of 16.9%) after 25 cycle numbers. The increased φ_e and the decreased φ_r all indicated that the cycle number had a great enhancement effect on the porosity alteration, which might increase the pore size and improve the connectivity. After the same number of cycles, the φ_e and φ_r values of the six cores exhibited different changes. Core sx-6 had the maximum φ_e increment of 2.76% (with an increase ratio of 243%) and φ_r decrement of 1.5% (with a decrease ratio of 25.4%), while core sx-1 had the minimum φ_e increment of 1.05% (with an 80.2% increase ratio) and φ_r decrement of 0.5% (with an 8.17% decrease ratio). This difference might be dependent on the cycle time, as the longer cycle time caused the matrix to completely shrink and swell to generate larger amounts of damage, eventually weakening the strength of the coal.

4.5. Crack Evolution Analysis. To intuitively characterize the results after some LCO₂ injection cycles, the photos and the corresponding sketch images of core sx-1 shown in Figure 10 were studied. A crack of small length was initially preexistent on the end surface; when the cycle number was 10 cycles, crack 1 had propagated for a certain distance under the effect of tension stress τ caused by the coupled mechanism between temperature stress and ice swelling force during the cyclic LCO₂ injection. As the cycle number increased, crack 1 extended continuously and crack 2 was generated at the weakened location along crack 1 when the cycle number reached 20 cycles. After the cycle number reached 25 cycles, crack 2 had propagated slowly, and crack 1 finally extended through the whole end surface. This process might be influenced by several factors: the mineral distribution, the petrological structure, and/or the water content

and its leakage quantity. The more uneven mineral distribution and the more complex petrological structure caused the cold to conduct less uniformly, resulting in some temperature stress to be produced among the contact points among the particles. The larger the amount of saturated water in the crack there is, the greater the ice volume preparation and the more violent the ice-wedge effect is. Under the cyclically coupled effect of temperature stress and ice-swelling force, the crack length was increased, and the connectivity between the cracks was enhanced; finally, the coal porosity was improved.

Analyses were performed regarding the variation in the different types of water, the change of spectral area, and the porosity, and some significant results were obtained. However, some research gaps still existed and were not explored, for instance, the relationship between the three types of water variation and the porosity, the relationships between the cycle parameters and the porosity, and the optimal application range of the different cycle parameters. Thus, many works will be carried out in future studies to improve the mechanistic understanding of these processes.

5. Conclusions

Several conclusions were made:

- (1) The T_2 spectra under saturation and centrifugation conditions obtained by LF-NMR with different cycle parameters were analyzed. As the cycle number increased, the AW values of all the cores decreased with different amplitudes while the CW and BW values increased adversely and their increase ratio variations were not independent but were influenced mutually.
- (2) The water increase ratios were positively correlated to the cycle number. Larger cycle numbers could freeze the saturated water and shrink the coal matrix more times, inducing more “unallowed damages or deformations” to form and accumulate with circulation,

which would cause many transformations to occur among pores with different sizes.

- (3) The concatenated I_{sa1} values were fitted as two different polynomial curves with fit coefficients more than 0.98, and the concatenated I_{sa2} values were fitted as an exponential curve with fit coefficient more than 0.95. The increased I_{sa1} and decreased I_{sa2} of the six cores all indicated that the pore volumes were magnified much more as the cycle number increased. Moreover, as the cycle time increased, I_{sa1} values approximately displayed a “rapid increase-slowly increase” tendency, while I_{sa2} approximately showed a singular “increase-decrease” tendency for short cycles and double “increase-decrease” trends for long cycles.
- (4) The positive relationship between the IWS values and cycle numbers was consistent with the tendency of increased amplitude and widened coverage of T_2 spectra under the saturation, whereas the negative relationship between the FWS value and cycle number indicated that free pore volume and space increased after the cyclic LCO₂ treatment. Moreover, the linear fit curves between the two corresponding concatenated values and cycle number were fitted well with a fit coefficient more than 0.95.
- (5) All the φ_e values were positively correlated to the cycle parameters and had a “slow increase-rapid increase” tendency whereas the φ_r values were negatively correlated to the cycle parameters and showed a “slow decrease-rapid decrease” trend. These variations indicated that the longer cycle time caused the matrix to completely shrink and swell, causing greater amounts of damages and weakening the strength of coals, and the cycle number also had a great enhancement effect on the porosity alteration, which might increase the pore size and improve the connectivity.

Conflicts of Interest

The authors declare that they have no conflicts of interest.

Acknowledgments

This work was financially supported by the National Natural Science Foundation of China (51774278, 51274195, and U1361106), the Natural Science Foundation of Jiangsu Province (BK20170001), the National Major Scientific Instrument and Equipment Development Project (2013YQ17046309), and the State Key Laboratory of Coal Resources and Safe Mining, China University of Mining and Technology (SKLCRSM14X02).

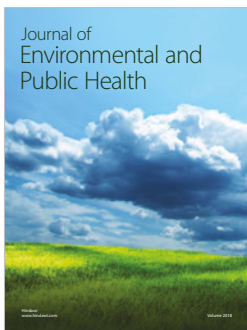
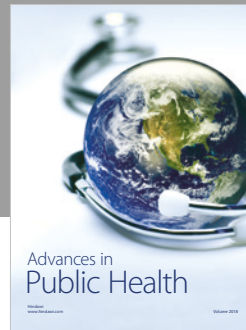
References

- [1] T. A. Moore, “Coalbed methane: a review,” *International Journal of Coal Geology*, vol. 101, pp. 36–81, 2012.

- [2] I. Palmer, “Coalbed methane completions: a world view,” *International Journal of Coal Geology*, vol. 82, no. 3-4, pp. 184–195, 2010.
- [3] A. Shahtalebi, C. Khan, A. Dmyterko, P. Shukla, and V. Rudolph, “Investigation of thermal stimulation of coal seam gas fields for accelerated gas recovery,” *Fuel*, vol. 180, pp. 301–313, 2016.
- [4] D. Ritter, D. Vinson, E. Barnhart et al., “Enhanced microbial coalbed methane generation: a review of research, commercial activity, and remaining challenges,” *International Journal of Coal Geology*, vol. 146, pp. 28–41, 2015.
- [5] C. Ö. Karacan, F. A. Ruiz, M. Cotè, and S. Phipps, “Coal mine methane: a review of capture and utilization practices with benefits to mining safety and to greenhouse gas reduction,” *International Journal of Coal Geology*, vol. 86, no. 2-3, pp. 121–156, 2011.
- [6] J. Xu, C. Zhai, and L. Qin, “Mechanism and application of pulse hydraulic fracturing in improving drainage of coalbed methane,” *Journal of Natural Gas Science and Engineering*, vol. 40, pp. 79–90, 2017.
- [7] G. Ni, W. Cheng, B. Lin, and C. Zhai, “Experimental study on removing water blocking effect (WBE) from two aspects of the pore negative pressure and surfactants,” *Journal of Natural Gas Science and Engineering*, vol. 31, pp. 596–602, 2016.
- [8] T. Liu, B. Lin, and W. Yang, “Impact of matrix–fracture interactions on coal permeability: model development and analysis,” *Fuel*, vol. 207, pp. 522–532, 2017.
- [9] Q. I. Zou, B. q. Lin, T. Liu, X. c. Hu, and C. s. Zheng, “Variations in coalbed gas content, initial gas desorption property and coal strength after drilling-slotting integration technique and gas drainage: insight into pore characteristics,” *International Journal of Oil, Gas and Coal Technology*, vol. 15, no. 3, pp. 235–266, 2017.
- [10] J. C. Pashin, P. E. Clark, M. R. McIntyre-Redden et al., “SECARB CO₂ injection test in mature coalbed methane reservoirs of the Black Warrior basin, Blue Creek Field, Alabama,” *International Journal of Coal Geology*, vol. 144-145, pp. 71–87, 2015.
- [11] B. Meier and S. Sharma, “Using stable carbon isotopes to track potential leakage of carbon dioxide: example from an enhanced coal bed methane recovery site in West Virginia, USA,” *International Journal of Greenhouse Gas Control*, vol. 41, pp. 107–115, 2015.
- [12] W. D. Gunter, M. J. Mavor, and J. R. Robinson, “CO₂ storage and enhanced methane production: field testing at Fenn-Big Valley, Alberta, Canada, with application,” in *Proceeding of the 7th International Conference on Greenhouse Gas Control Technologies*, Vancouver, Canada, September 2004.
- [13] M. M. Reynolds, R. S. Ku, J. B. Vertz, and Z. D. Stashko, “First field application in Canada of carbon dioxide separation for hydraulic fracture flow back operations,” in *SPE 167197-MS, SPE Unconventional Resources Conference Canada*, Calgary, Alberta, Canada, November 2013.
- [14] S. Wong, D. Law, X. Deng et al., “Enhanced coalbed methane and CO₂ storage in anthracitic coals—micro-pilot test at south Qinshui, Shanxi, China,” *International Journal of Greenhouse Gas Control*, vol. 1, no. 2, pp. 215–222, 2007.
- [15] J. Liu, L. Sun, X. Wu, and J. Yao, “Feasibility of combination of CO₂ geological storage with geothermal-type water-soluble gas recovery in Yinggehai basin, China,” *International Journal of Greenhouse Gas Control*, vol. 45, pp. 139–149, 2016.

- [16] M. Fujioka, S. Yamaguchi, and M. Nako, "CO₂-ECBM field tests in the Ishikari Coal Basin of Japan," *International Journal of Coal Geology*, vol. 82, no. 3-4, pp. 287-298, 2010.
- [17] S. Yamaguchi, K. Ohga, M. Fujioka, and M. Nako, "History matching on micro-pilot tests of CO₂ sequestration and ECBM in the Ishikari Coal Field," *Journal of the Japan Institute of Energy*, vol. 86, no. 2, pp. 80-86, 2007.
- [18] H. Wen, Z. Li, J. Deng et al., "Influence on coal pore structure during liquid CO₂-ECBM process for CO₂ utilization," *Journal of CO₂ Utilization*, vol. 21, pp. 543-552, 2017.
- [19] J. Xu, C. Zhai, S. Liu, L. Qin, and Y. Sun, "Feasibility investigation of cryogenic effect from liquid carbon dioxide multi cycle fracturing technology in coalbed methane recovery," *Fuel*, vol. 206, pp. 371-380, 2017.
- [20] Y. Cao, J. Zhang, H. Zhai, G. Fu, L. Tian, and S. Liu, "CO₂ gas fracturing: a novel reservoir stimulation technology in low permeability gassy coal seams," *Fuel*, vol. 203, pp. 197-207, 2017.
- [21] R. Sander, L. D. Connell, Z. Pan, M. Camilleri, D. Heryanto, and N. Lupton, "Core flooding experiments of CO₂ enhanced coalbed methane recovery," *International Journal of Coal Geology*, vol. 131, pp. 113-125, 2014.
- [22] H. Xu, W. Chu, X. Huang, W. Sun, C. Jiang, and Z. Liu, "CO₂ adsorption-assisted CH₄ desorption on carbon models of coal surface: a DFT study," *Applied Surface Science*, vol. 375, pp. 196-206, 2016.
- [23] D. N. Espinoza and J. C. Santamarina, "Clay interaction with liquid and supercritical CO₂: the relevance of electrical and capillary forces," *International Journal of Greenhouse Gas Control*, vol. 10, pp. 351-362, 2012.
- [24] S. Gao, Y. Wang, L. Jia, H. Wang, J. Yuan, and X. Wang, "CO₂-H₂O-coal interaction of CO₂ storage in coal beds," *International Journal of Mining Science and Technology*, vol. 23, no. 4, pp. 525-529, 2013.
- [25] W. Li, P. L. Younger, Y. Cheng et al., "Addressing the CO₂ emissions of the world's largest coal producer and consumer: lessons from the Haishiwan Coalfield, China," *Energy*, vol. 80, pp. 400-413, 2015.
- [26] N. H. Mohd Yasin, T. Maeda, A. Hu, C.-P. Yu, and T. K. Wood, "CO₂ sequestration by methanogens in activated sludge for methane production," *Applied Energy*, vol. 142, pp. 426-434, 2015.
- [27] J. Xu, C. Zhai, S. Liu, L. Qin, and S. Wu, "Pore variation of three different metamorphic coals by multiple freezing-thawing cycles of liquid CO₂ injection for coalbed methane recovery," *Fuel*, vol. 208, pp. 41-51, 2017.
- [28] P. A. Hale and A. Shakoor, "A laboratory investigation of the effects of cyclic heating and cooling, wetting and drying, and freezing and thawing on the compressive strength of selected sandstones," *Environmental and Engineering Geoscience*, vol. 9, no. 2, pp. 117-130, 2003.
- [29] C. Zhai, S. Wu, S. Liu, L. Qin, and J. Xu, "Experimental study on coal pore structure deterioration under freeze-thaw cycles," *Environmental Earth Sciences*, vol. 76, no. 15, p. 507, 2017.
- [30] J. Q. Mu, X. J. Pei, R. Q. Huang, N. Rengers, and X. Q. Zou, "Degradation characteristics of shear strength of joints in three rock types due to cyclic freezing and thawing," *Cold Regions Science and Technology*, vol. 138, pp. 91-97, 2017.
- [31] Q. Liu, S. Huang, Y. Kang, and X. Liu, "A prediction model for uniaxial compressive strength of deteriorated rocks due to freeze-thaw," *Cold Regions Science and Technology*, vol. 120, pp. 96-107, 2015.
- [32] X. Zhang, L. Wang, and J. Zhang, "Mechanical behavior and chloride penetration of high strength concrete under freeze-thaw attack," *Cold Regions Science and Technology*, vol. 142, pp. 17-24, 2017.
- [33] L. Qin, C. Zhai, S. Liu, J. Xu, Z. Tang, and G. Yu, "Failure mechanism of coal after cryogenic freezing with cyclic liquid nitrogen and its influences on coalbed methane exploitation," *Energy & Fuels*, vol. 30, no. 10, pp. 8567-8578, 2016.
- [34] L. Liu, S. Wu, H. Chen, and Z. Haitao, "Numerical investigation of the effects of freezing on micro-internal damage and macro-mechanical properties of cement pastes," *Cold Regions Science and Technology*, vol. 106-107, pp. 141-152, 2014.
- [35] P. Wang, J. Xu, X. Fang, P. Wang, G. Zheng, and M. Wen, "Ultrasonic time-frequency method to evaluate the deterioration properties of rock suffered from freeze-thaw weathering," *Cold Regions Science and Technology*, vol. 143, pp. 13-22, 2017.
- [36] M. Molero, S. Aparicio, G. Al-Assadi, M. J. Casati, M. G. Hernández, and J. J. Anaya, "Evaluation of freeze-thaw damage in concrete by ultrasonic imaging," *NDT & E International*, vol. 52, pp. 86-94, 2012.
- [37] J. Park, C. U. Hyun, and H. D. Park, "Changes in microstructure and physical properties of rocks caused by artificial freeze-thaw action," *Bulletin of Engineering Geology and the Environment*, vol. 74, no. 2, pp. 555-565, 2015.
- [38] M. Mutluturk, R. Altindag, and G. Turk, "A decay function model for the integrity loss of rock when subjected to recurrent cycles of freezing-thawing and heating-cooling," *International Journal of Rock Mechanics and Mining Sciences*, vol. 41, no. 2, pp. 237-244, 2004.
- [39] J. Zhao, H. Xu, D. Tang, J. P. Mathews, S. Li, and S. Tao, "Coal seam porosity and fracture heterogeneity of macrolithotypes in the Hancheng Block, eastern margin, Ordos Basin, China," *International Journal of Coal Geology*, vol. 159, pp. 18-29, 2016.
- [40] Q. Li, B. Lin, and C. Zhai, "A new technique for preventing and controlling coal and gas outburst hazard with pulse hydraulic fracturing: a case study in Yuwu coal mine, China," *Natural Hazards*, vol. 75, no. 3, pp. 2931-2946, 2015.
- [41] Q. Zou and B. Lin, "Modeling the relationship between macro- and meso-parameters of coal using a combined optimization method," *Environmental Earth Sciences*, vol. 76, no. 14, p. 479, 2017.
- [42] T. Liu, B. Lin, W. Yang et al., "Dynamic diffusion-based multi-field coupling model for gas drainage," *Journal of Natural Gas Science and Engineering*, vol. 44, pp. 233-249, 2017.
- [43] T. Xia, F. Zhou, J. Liu, S. Hu, and Y. Liu, "A fully coupled coal deformation and compositional flow model for the control of the pre-mining coal seam gas extraction," *International Journal of Rock Mechanics and Mining Sciences*, vol. 72, pp. 138-148, 2014.
- [44] L. D. Connell, R. Sander, M. Camilleri, D. Heryanto, Z. Pan, and N. Lupton, "Nitrogen enhanced drainage of CO₂ rich coal seams for mining," *International Journal of Mining Science and Technology*, vol. 27, no. 5, pp. 755-761, 2017.
- [45] C. Zheng, M. Kizil, Z. Chen, and S. Aminossadati, "Effects of coal damage on permeability and gas drainage performance,"

- International Journal of Mining Science and Technology*, vol. 27, no. 5, pp. 783–786, 2017.
- [46] T. Teng, F. Gao, Y. N. Gao, and Z. Z. Zhang, “Experimental study of micro-damage and fracturing characteristics on raw coal under cyclic pneumatic hydraulic loading,” *Journal of China University of Mining & Technology*, vol. 46, pp. 306–311, 2017.
- [47] J. Yang, W. Chen, D. Yang, and H. Tian, “Investigating the permeability of marble under moderate pressure and temperature,” *Geofluids*, vol. 2017, 8 pages, 2017.
- [48] S. Chattaraj, D. Mohanty, T. Kumar, and G. Halder, “Thermodynamics, kinetics and modeling of sorption behaviour of coalbed methane – a review,” *Journal of Unconventional Oil and Gas Resources*, vol. 16, pp. 14–33, 2016.
- [49] S. Giffin, R. Littke, J. Klaver, and J. L. Urai, “Application of BIB-SEM technology to characterize macropore morphology in coal,” *International Journal of Coal Geology*, vol. 114, pp. 85–95, 2013.
- [50] W. Li, H. Liu, and X. Song, “Multifractal analysis of Hg pore size distributions of tectonically deformed coals,” *International Journal of Coal Geology*, vol. 144–145, pp. 138–152, 2015.
- [51] J. S. Bae, S. K. Bhatia, V. Rudolph, and P. Massarotto, “Pore accessibility of methane and carbon dioxide in coals,” *Energy & Fuels*, vol. 23, no. 6, pp. 3319–3327, 2009.
- [52] Y. Yao and D. Liu, “Comparison of low-field NMR and mercury intrusion porosimetry in characterizing pore size distributions of coals,” *Fuel*, vol. 95, pp. 152–158, 2012.
- [53] D. Wildenschild and A. P. Sheppard, “X-ray imaging and analysis techniques for quantifying pore-scale structure and processes in subsurface porous medium systems,” *Advances in Water Resources*, vol. 51, pp. 217–246, 2013.
- [54] A. P. Radlinski, M. Mastalerz, A. L. Hinde et al., “Application of SAXS and SANS in evaluation of porosity, pore size distribution and surface area of coal,” *International Journal of Coal Geology*, vol. 59, no. 3–4, pp. 245–271, 2004.
- [55] L. Qin, C. Zhai, S. Liu, J. Xu, G. Yu, and Y. Sun, “Changes in the petrophysical properties of coal subjected to liquid nitrogen freeze-thaw – a nuclear magnetic resonance investigation,” *Fuel*, vol. 194, pp. 102–114, 2017.
- [56] R. L. Kleinberg, W. E. Kenyon, and P. P. Mitra, “Mechanism of NMR relaxation of fluids in rock,” *Journal of Magnetic Resonance, Series A*, vol. 108, no. 2, pp. 206–214, 1994.
- [57] J. Xu, C. Zhai, S. Liu, L. Qin, and R. Dong, “Investigation of temperature effects from LCO₂ with different cycle parameters on the coal pore variation based on infrared thermal imagery and low-field nuclear magnetic resonance,” *Fuel*, vol. 215, pp. 528–540, 2018.
- [58] Y. Cai, D. Liu, Z. Pan, Y. Yao, J. Li, and Y. Qiu, “Petrophysical characterization of Chinese coal cores with heat treatment by nuclear magnetic resonance,” *Fuel*, vol. 108, pp. 292–302, 2013.
- [59] A. Dillinger and L. Esteban, “Experimental evaluation of reservoir quality in Mesozoic formations of the Perth Basin (Western Australia) by using a laboratory low field nuclear magnetic resonance,” *Marine and Petroleum Geology*, vol. 57, pp. 455–469, 2014.
- [60] O. B. Olatinsu, D. O. Olorode, B. Clennell, L. Esteban, and M. Josh, “Lithotype characterizations by nuclear magnetic resonance (NMR): a case study on limestone and associated rocks from the eastern Dahomey Basin, Nigeria,” *Journal of African Earth Sciences*, vol. 129, pp. 701–712, 2017.
- [61] C. X. Ning, Z. X. Jiang, and Z. Y. Gao, “Quantitative evaluation of pore connectivity with nuclear magnetic resonance and high pressure mercury injection: a case study of the lower section of E s3 in Zhanhua sag,” *Journal of China University of Mining & Technology*, vol. 46, pp. 559–566, 2017.
- [62] N. Golsanami, J. Sun, and Z. Zhang, “A review on the applications of the nuclear magnetic resonance (NMR) technology for investigating fractures,” *Journal of Applied Geophysics*, vol. 133, pp. 30–38, 2016.



Hindawi

Submit your manuscripts at
www.hindawi.com

